Three-dimensional heat transfer effects in external layers of a magnetized neutron star

Ilya A. Kondratyev,[1,2]★ Sergey. G. Moiseenko,[1,2] Gennady S. Bisnovatyi-Kogan[1,3,4] and Maria V. Glushikhina[1]

[1]*Space Research Institute, Russian Academy of Sciences, Profsoyuznaya st. 84/32, Moscow 117997, Russia*
[2]*Department of Physics, National Research University Higher School of Economics, Staraya Basmannaya st. 21/4 b.5, Moscow 105066, Russia*
[3]*National Research Nuclear University MEPhI, Kashirskoe sh., 31, Moscow 115409, Russia*
[4]*Moscow Institute of Physics and Technology, Institutskiy per. 9, Dologoprudny, Moscow 141701, Russia*

ABSTRACT

Determination of a magnetic field structure on a neutron star (NS) surface is an important problem of a modern astrophysics. In a presence of strong magnetic fields, a thermal conductivity of a degenerate matter is anisotropic. In this paper, we present 3D anisotropic heat transfer simulations in outer layers of magnetized NSs, and construct synthetic thermal light curves. We have used a different from previous works tensorial thermal conductivity coefficient of electrons, derived from the analytical solution of the Boltzmann equation by the Chapman–Enskog method. We have obtained an NS surface temperature distribution in presence of dipole-plus-quadrupole magnetic fields. We consider a case, in which magnetic axes of a dipole and quadrupole components of the magnetic field are not aligned. To examine observational manifestations of such fields, we have generated thermal light curves for the obtained temperature distributions using a composite blackbody model. It is shown that the simplest (only zero-order spherical function in quadrupole component) non-coaxial dipole-plus-quadrupole magnetic field distribution can significantly affect the thermal light curves, making pulse profiles non-symmetric and amplifying pulsations in comparison to the pure-dipolar field.

Key words: conduction – magnetic fields – radiation mechanisms: thermal – methods: numerical – stars: neutron.

1 INTRODUCTION

A strength of magnetic fields on the neutron star (NS) surface may reach $\sim 10^{12-13}$ and 10^{15} G in magnetars. One of possible ways to observe surface magnetic fields is an observation of a thermal radiation in the soft X-ray band (e.g. Pons et al. 2002; Page, Geppert & Weber 2006; Haberl 2007). X-ray observatories, such as *ROSAT*, *Chandra*, and *XMM–Newton*, have detected thermally emitting compact objects. Seven nearby radio-silent XDINSs (X-ray Dim Isolated Neutron Star) are called 'magnificent seven' (see e.g. Turolla 2009 for a review). Periodic changes in spectra of such NSs may indicate to non-uniform temperature distributions on their surfaces. Such heterogeneities are determined by an anisotropic thermal conductivity of degenerate matter in presence of a strong magnetic field (e.g. Bisnovatyi-Kogan, Kulikov & Chechetkin 1976). Outer layers of an NS consist of plasma with degenerate electrons, and non-degenerate non-relativistic nuclei. The pressure is determined mostly by the electrons, and the matter can form a state of the Coulomb crystal or liquid, and a heat transfers mostly by the electrons as well. The thermal conductivity is suppressed across the magnetic field lines. A degree of its suppression across the magnetic field is determined by the so-called magnetization parameter $\omega\tau$, where τ is the average time between electron–nuclei collisions, where $\omega = eB/m_e^* c$ is the electron cyclotron plasma frequency, with

$m_e^* = m_e \sqrt{1 + p_{fe}^2/m_e^2 c^2}$ as an effective relativistic electron mass, and $p_{fe} = \hbar(3\pi^2 n_e)^{1/3}$ as an electron Fermi momentum, e as the electron charge, c as the speed of light, and $\hbar$ as the reduced Planck constant. A thermal conductivity tensor, as well as other kinetic coefficients, for the plasma with degenerate electrons are derived in a series of papers by Bisnovatyi-Kogan & Glushikhina (2018a,b) and Glushikhina (2020), from the solution of the Boltzmann equation by the Chapman–Enskog method. The degree of the heat flux depression across the field is stronger, than in previous works (e.g. Flowers & Itoh 1976; Urpin & Yakovlev 1980), where a ratio between heat conductivities along and across the magnetic field lines is connected by the relation $\frac{\kappa_\parallel}{\kappa_\perp} = 1 + (\omega\tau)^2$.

Heat transfer processes in the outer layers of the NS with the coaxial dipolar and quadrupolar fields were considered earlier in the paper Kondratyev et al. (2020), hereinafter referred as Paper I, where the model of the magnetized envelope and used numerical technique are described in details. In this paper, we obtain stationary temperature distribution in outer layers of NSs in the presence of dipole and quadrupole fields, whose axes are not aligned. We solved numerically a three-dimensional heat transfer equation in the NS crust for the densities $\rho = 10^{10}$ to 2×10^{14} g cm^{-3} using our T_s–T_b relationship for the outer magnetized envelope, which connects temperature T_b on the $\rho = 10^{10}$ g cm^{-3} with the temperature T_s on the NS surface, similarly to Gudmundsson, Pethick & Epstein (1983), Potekhin & Yakovlev (2001), and Kondratyev et al. (2020). We have built 'T_s–T_b' relationship adopting thermal conductivities from Bisnovatyi-Kogan & Glushikhina (2018a) in Paper I. In a 2D case, a

★ E-mail: mrkondratyev95@gmail.com

problem about finding a stationary solution of the NS temperature is was studied by several authors Geppert, Kuker & Page (2004), Perez-Azorin, Miralles & Pons (2006), Geppert, Kuker & Page (2006), and a 2D NS cooling problem was considered by Aguilera, Pons & Miralles (2008), Pons, Miralles & Geppert (2009), and Vigano et al. (2013) (see also a review by Potekhin, Pons & Page 2015). In this work, we restrict ourselves to consideration of stationary temperature distributions. We mention also a recent review Pons & Vigano (2019) on numerical simulations of the magnetic field and thermal evolution of an isolated NS.

The paper is organized as follows. In second part of this work, we review a basic physical input, such as properties of heat transfer, magnetic field configurations, and equation of state. In the third part, we briefly discuss a thermal structure of a magnetized outer envelope. In the fourth part, a formulation of the boundary problem for the 3D heat transfer equation is given. In the fifth part, we present the results about the temperature distributions, and thermal light curves. In appendices, we discuss radiative opacities, and numerical algorithm used in the calculations.

2 PHYSICAL INPUT

2.1 Heat transfer in presence of a magnetic field

The temperature distribution is determined by the heat transfer equation

$$C\frac{\partial T}{\partial t} = \nabla \cdot \hat{\boldsymbol{\kappa}} \cdot \nabla T + f, \tag{1}$$

where C is a heat capacity, $\hat{\boldsymbol{\kappa}}$ is a thermal conductivity tensor, f is defined by heat sources and sinks (Joule heating, neutrino emission, etc.). We look for a stationary solution ($\frac{\partial T}{\partial t} = 0$) in absence of sources and sinks, with $f = 0$.

The thermal conductivity tensor $\hat{\boldsymbol{\kappa}}$ for strongly degenerate electrons in the magnetic field was obtained by Bisnovatyi-Kogan & Glushikhina (2018a) using the Chapman–Enskog method for the Boltzmann equation. This tensor takes into account heat fluxes along and across the magnetic field as well as the Hall heat flux. In the Cartesian coordinates, it is written as follows:

$$\begin{cases} \kappa_{ij} = \frac{k_B^2 T n_e}{m_e^*} \tau \left(\kappa^{(1)}\delta_{ij} + \kappa^{(2)}\varepsilon_{ijk}\frac{B_k}{B} + \kappa^{(3)}\frac{B_i B_j}{B^2} \right) \\ \kappa^{(1)} = \frac{5\pi^2}{6} \left(\frac{1}{1+(\omega\tau)^2} - \frac{6}{5}\frac{(\omega\tau)^2}{(1+(\omega\tau)^2)^2} \right) \\ \kappa^{(2)} = -\frac{4\pi^2}{3}\omega\tau \left(\frac{1}{1+(\omega\tau)^2} - \frac{3}{4}\frac{(\omega\tau)^2}{(1+(\omega\tau)^2)^2} \right) \\ \kappa^{(3)} = \frac{5\pi^2}{6}(\omega\tau)^2 \left(\frac{1}{1+(\omega\tau)^2} + \frac{6}{5}\frac{1}{(1+(\omega\tau)^2)^2} \right) \end{cases}, \tag{2}$$

where $n_e = \frac{\rho Z}{A m_u}$ is an electron number density, Z is the nucleus (ion) charge number, and A is the mass number; $\tau = \frac{3}{32\pi^2}\frac{h^3}{m_e^* Z e^4 \Lambda}$ is an average time between electron–nuclei collisions, k_B is the Boltzmann constant, h is the Planck constant, Λ is the Coulomb logarithm (see e.g. Braginskii 1957), we adopt its value from the paper by Yakovlev & Urpin (1980). Parameter $\omega\tau$ changes drastically in the crust and the envelope of the NS. Its value is close to unity at $\rho \sim 10^{10}$ g cm^{-3}, $B \sim 10^{13}$ G, and approximately is changing $\omega\tau \sim B/\rho^{2/3}$ for the ultrarelativistic degenerate electron gas in the crust. As it follows from (2), the heat conductivity coefficients across and along the magnetic field may be written as following:

$$\begin{cases} \kappa_{e\perp} = \frac{k_B^2 T n_e}{m_e^*}\tau\kappa^{(1)}, \\ \kappa_{e\parallel} = \frac{k_B^2 T n_e}{m_e^*}\tau\left(\kappa^{(1)} + \kappa^{(3)}\right). \end{cases} \tag{3}$$

Note here one important detail. The value of a thermal conductivity of a strongly degenerate electron gas along the magnetic field $\kappa'_{e\parallel}$,

from papers by Flowers & Itoh (1976) and Urpin & Yakovlev (1980), has a different numerical coefficient from (3) for $\kappa_{e\parallel}$:

$$\kappa'_{e\parallel} = \frac{\pi^2}{3}\frac{k_B^2 T n_e}{m_e^*}\tau, \tag{4}$$

which is 2.5 times less than in (2). In a large amount of astrophysical studies, electron thermal conductivity coefficient is used in that setting. Expression (4) is used for the thermal electron conductivity in metals in laboratory, in the condition of zero electron diffusion velocity (electrical current).

This discrepancy can be shown clear for the thermal conduction coefficient in the absence of a magnetic field, as well as the one along the magnetic field. As it follows from the Boltzmann equation in the Lorentz approximation, the heat flux $\boldsymbol{q}$, and the average electron velocity $\langle\boldsymbol{v_e}\rangle$ are defined as (e.g. Bisnovatyi-Kogan 2001)

$$\begin{aligned} \boldsymbol{q} &= -\frac{640 k_B}{\Lambda}\frac{m_e(k_B T)^4}{n_N Z^2 e^4 h^3}\left(G_5 - \frac{1}{2}\frac{G_{5/2}}{G_{3/2}}G_4\right)\cdot\nabla T \\ &\quad - \frac{128}{\Lambda}\frac{m_e(k_B T)^5}{n_N Z^2 e^4 h^3}\frac{G_{5/2}}{G_{3/2}}G_4\cdot\boldsymbol{d_e} \\ \langle\boldsymbol{v_e}\rangle &= -\frac{128 k_B}{\Lambda}\frac{m_e(k_B T)^3}{n_N n_e Z^2 e^4 h^3}\left(G_4 - \frac{5}{8}\frac{G_{5/2}}{G_{3/2}}G_3\right)\cdot\nabla T \\ &\quad - \frac{32}{\Lambda}\frac{m_e(k_B T)^4}{n_N n_e Z^2 e^4 h^3}\frac{G_{5/2}}{G_{3/2}}G_3\cdot\boldsymbol{d_e}, \end{aligned} \tag{5}$$

where n_N is a nuclei number density, a vector $\boldsymbol{d_e}$ determines a diffusive flux (see Bisnovatyi-Kogan & Glushikhina 2018b). A function $G_n = G_n(x_0)$ is the Fermi function, $x_0 = \frac{p_{fe}^2}{2m_e k_B T}$.

In laboratory conditions, when the electrical conductivity is small, and electrical currents are damped rapidly, so that the current density $\boldsymbol{j_e} \sim \langle\boldsymbol{v_e}\rangle = 0$ in (5). This simplification leads to linear connection between the diffusion vector $\boldsymbol{d_e}$ and the temperature gradient. It leads to expression (4), which also follows from an approximate theory of heat conductivity and diffusion, based on the mean free path. In a more general case in the presence of the magnetic field, it leads to the simple dependence of the thermal conductivity tensor on the magnetization parameter.

In outer layers of magnetized NSs, the electric currents are substantial, and thermoelectric effects take place Blandford, Applegate & Hernquist (1983), so that the average velocity is not equal to zero any more, and heat transfer should be considered together with diffusion (see Bisnovatyi-Kogan & Glushikhina 2018b for details). The expression for the heat flux we use is connected only with a temperature gradient, when the diffusion vector $\boldsymbol{d_e} = 0$. This approach is approximate as well, and a consistent consideration of thermoelectric processes has to be done. Nevertheless, our axisymmetric heat transfer simulations from Paper I are in good agreement with the ones by Geppert et al. (2004) for core-dipolar magnetic fields.

2.2 Magnetic field configuration

We consider dipole and quadrupole configurations of the magnetic field, which are defined by the following formulae. For the dipole we have (e.g. Landau & Lifshitz 1988)

$$\boldsymbol{B} = \frac{B_{pd}R_{NS}^3}{2}\frac{3(\boldsymbol{d}\cdot\boldsymbol{r})\boldsymbol{r} - \boldsymbol{d}r^2}{r^5} \tag{6}$$

where B_{pd} is the value of a magnetic induction at the magnetic pole on the NS surface, $\boldsymbol{d}$ is a unit vector in the direction of the magnetic dipole, and R_{NS} is an NS radius. For the quadrupole configuration,

with a quadrupole momentum in the direction of z axis, we have

$$\boldsymbol{B} = B_{\mathrm{pq}} R_{\mathrm{NS}}^4 \left(\frac{r^2 - 5z^2}{2r^7} \boldsymbol{r} - \frac{\boldsymbol{e_z} z}{r^5} \right), \tag{7}$$

where $\boldsymbol{e_z}$ is a unit vector along a z-axis. In the subsequent consideration, we consider a combination of these two field configuration, with different values of B_{pd} and B_{pq}, and different angles between vectors $\boldsymbol{d}$ and $\boldsymbol{e_z}$, in the envelope, and in the crust of NS.

2.3 Equation of state and envelope model

Density appears explicitly in the thermal conductivity tensor (2). We have built an NS model by solving Tolman–Oppenheimer–Volkoff equations of the hydrostatic equilibrium to get a density profile in the crust. For the NS interior, we used moderately stiff equation of state (EOS) SLy4 of Douchin & Haensel (2001), which is based on microscopic calculations with an effective nuclear potential from Chabanat et al. (1997). The used EOS describes consistently both the crust and the core. We have chosen central density $\rho_c = 1 \times 10^{15}$ g cm^{-3}. The NS mass is $M_{\mathrm{NS}} = 1.42\,\mathrm{M}_\odot$, where $\mathrm{M}_\odot$ is the Solar mass, the inner and outer radii of the NS crust are $R_{\mathrm{in}} = 10.59$ km at $\rho = \rho_{\mathrm{in}} = 2 \times 10^{14}$ g cm^{-3} and $R_{\mathrm{out}} = R_{\mathrm{NS}} = 11.62$ km at $\rho = 10^{10}$ g cm^{-3}, respectively. We have taken into account a neutronization of the matter in the crust with effective A and Z. Those values are taken from Baym, Bethe & Pethick (1971b) for the density $\rho < \rho_{\mathrm{drip}}$ and from Baym, Pethick & Sutherland (1971a) for $\rho > \rho_{\mathrm{drip}}$, where $\rho_{\mathrm{drip}} = 4 \times 10^{11}$ g cm^{-3} is the neutron drip density.

The outer envelope of the NS is a thin near-surface layer (~ 100 m in depth) of plasma, which extends from the NS crust to the radiative surface. It consists of partially degenerate electrons and non-degenerate iron nuclei. We have neglected the effects of non-ideality and quantizing magnetic fields on the EOS and assumed ideal fully ionized plasma of iron ($Z = 26$, $A = 56$) with non-degenerate non-relativistic nuclei, and degenerate relativistic electrons:

$$P = P_{\mathrm{n}}^{(N)} + P_{\mathrm{d}}^{(e)},$$

where $P_{\mathrm{n}}^{(N)} = n_N k_B T$ is an ion pressure, indices 'n', 'd' correspond to non-degenerate and degenerate gases, respectively. The pressure of the electrons at arbitrary degree of the degeneracy and relativism can be written in terms of Fermi–Dirac integrals:

$$P_{\mathrm{d}}^{(e)} = \frac{(2m_e)^{3/2}}{3\pi^2 \hbar^3 \beta^{5/2}} \left(I_{3/2}(\chi, \tau) + \frac{\tau}{2} I_{5/2}(\chi, \tau) \right), \tag{8}$$

where $\beta = (k_B T)^{-1}$, $\chi = \beta \mu_{id}^{(e)}$ is the electron chemical potential, normalized on $k_B T$, $\tau = (\beta m_e c^2)^{-1}$, and Fermi–Dirac integrals are defined as follows:

$$I_\nu(\chi, \tau) = \int_0^\infty \frac{u^\nu \sqrt{1 + \tau u/2}}{\exp(u - \chi) + 1} \, du, \tag{9}$$

here $u = \beta m_e c^2 (\sqrt{1 + \frac{p^2 c^2}{m_e^2 c^4}} - 1)$, and p is an electron momentum. We used the analytical approximations for the Fermi–Dirac integrals from Blinnikov et al. (1996). For the electron chemical potential χ, we use a non-relativistic analytical approximation from Antia (1993) with relativistic corrections adopted from Chabrier & Potekhin (1998).

In a thin envelope, the radial temperature gradient and the radial heat flux are much larger than the azimuthal ones. Therefore, the heat flux approximately is assumed to be only radial through the envelope. Such approach leads to the local, one-dimensional plane-parallel model of the envelope thermal structure. Thus, the temperature distribution in an envelope region can be calculated separately from the crust. To solve the problem self-consistently, it is necessary to

find a common solution for the envelope and the crust, for a given temperature of the isothermal NS core my means, suggested by Geppert et al. (2004). The first step for finding this self-consistent solution is a calculation of the relation between a surface temperature T_s, and a temperature at the bottom of the envelope T_b with the fixed density ρ_b. This relation is constructed by solution of local one-dimensional heat transfer equation, with different microphysics input. Due to anisotropic heat transfer in presence of a strong magnetic field, the '$T_s - T_b$' relationship is a variable over the NS surface, depending on the magnetic field distribution. For non-magnetized NSs, '$T_s - T_b$' relationships were constructed in e.g. Gudmundsson et al. (1983) and Potekhin, Chabrier & Yakovlev (1997), and in Potekhin & Yakovlev (2001), Potekhin, Chabrier & Yakovlev (2007), and Pons et al. (2009) they were calculated for magnetized NSs (in the latter paper in 2D approach).

The thermal structure equation for the envelope reads (e.g. Gudmundsson et al. 1983; Potekhin & Yakovlev 2001):

$$\frac{dT}{dP} = \frac{3K}{16 g_s} \frac{T_s^4}{T^3}, \tag{10}$$

where T_s is a local surface temperature, $K = K(B, \theta_B, T, \rho)$ is an effective opacity, θ_B is a magnetic field inclination angle to the normal of the surface, $g_s = G M_{\mathrm{NS}} / (R_{\mathrm{NS}}^2 \sqrt{1 - r_g / R_{\mathrm{NS}}})$ is the surface gravity acceleration, with approximate account of GR effects (e.g. Gudmundsson et al. 1983; Van Riper 1988), G is the gravitational constant, and r_g is the NS gravitational radius.

The heat flux is determined by a sum of two processes: radiative and electron heat transfer. For the radiative opacity, we have taken into account free–free and bound–free transitions as well as an electron Thompson scattering for both non-degenerate and degenerate electrons. More detailed discussion can be found in Appendix A. The electron opacity can be derived from an analogy with a radiative heat transfer:

$$K_e = \frac{16\sigma T^3}{3\kappa_e \rho}. \tag{11}$$

Here, $\kappa_e = \kappa_{e\parallel} \cos^2 \theta_B + \kappa_{e\perp} \sin^2 \theta_B$ is a local effective value of the thermal conductivity coefficient (3) for degenerate electrons.

Equation (10) is solved as a Cauchy problem for the given values of surface temperature T_s and surface pressure P_s. The latter is calculated from Eddington approximation $P_s \approx \frac{2g_s}{3K(B, \theta_B, T_s, \rho_s)}$ (see Potekhin et al. 1997). We used the tabulated $T_s - T_b$ relationship for $\rho_b = 10^{10}$ g cm^{-3} to implement it in a radiative outer boundary condition for the heat transfer equation in the crust, which was presented and discussed in detail in Paper I.

3 A BOUNDARY-VALUE PROBLEM

After a fast stage of neutrino cooling, the core of the NS cools down slowly, and temperature distribution may be considered as a stationary one. So that, a thermal evolution of the NS could be considered as a sequence of cooling models with a stationary temperature distribution over the NS. The temperature is supposed to be constant through the core T_{core}, because of a large value of the heat conductivity, and to be equal to the value on the inner radius of the crust.

In a thin envelope, the radial temperature gradient and the radial heat flux are much larger than the azimuthal ones, which are not considered subsequently any more. In a thin low-mass envelope, the local heat flux F_s, from the NS unit surface, is supposed to be constant along the radius, varying only over the surface. The flux is also supposed to have a blackbody spectrum, and follows the Stephan–Boltzmann law $F_s(\theta, \phi) = \sigma T_s^4$, with $T_s(\theta, \phi)$ being the local surface NS temperature.

For a given core temperature T_{core}, the way of construction of thermal NS model, and its surface temperature $T_s(\theta, \phi)$ may be summarized in the following way.

1. Take a trial value of the surface temperature $T_s^{(1)}$, which determines uniquely the surface parameters, and local heat flux $F_s^{(1)}$. Using these parameters as boundary conditions for solution of the heat conduction equation in the envelope, we obtain the value of the temperature at the bottom of the envelope $T_b^{(1)}(\theta, \phi)$, and find T_s–T_b relationship.

2. The value is given for the core temperature T_{core} which is equal to the temperature at the inner crust with $r = R_{in}$, and $r = R_{out}$, as inner and outer radii of the crust. The local flux distribution $F_s^{(1)}(\theta, \phi)$ at the outer crust boundary is taken from the envelope structure. The conditions at the inner and outer boundaries are

$$T_{in} = T_{core}, \quad \kappa(\boldsymbol{B}, \rho, T)\nabla_r T|_{out} + F_s = 0, \tag{12}$$

In the spherical layer $R_{in} \leq r \leq R_{out}$, we solve the boundary-value problem for the heat transfer equation

$$\nabla \cdot \kappa(\boldsymbol{B}, \rho, T) \cdot \nabla T = 0 \tag{13}$$

with the boundary conditions (12). We calculate 3D model of the magnetized crust, and obtain distribution of the temperature on the outer crust boundary $T_{cr}^{(1)}(\theta, \phi)$.

3. In the self-consistent model, the temperature at the inner boundary of the envelope should coincide with the temperature at the outer boundary of the crust, so two distributions should coincide

$$T_b(\theta, \phi) = T_{cr}(\theta, \phi). \tag{14}$$

The iterations by Newton method are performed until the equality $T_b^{(i)}(\theta, \phi) = T_{cr}^{(i)}(\theta, \phi)$ will be fulfilled with a necessary precision. This procedure should be performed for each magnetic field distribution under investigation.

A heat transfer problem in the crust of a magnetized NS was solved numerically with our extension of the basic operators method (Ardeljan & Kosmachevskii 1995). 3D mesh analogues of main differential operators on an unstructured tetrahedral mesh were derived by Kondratyev & Moiseenko (2019); numerical method for obtaining a self-consistent solution of the heat transfer equation in the crust is developed in Paper I; and the numerical implementation of the method is briefly discussed in Appendix B of this paper.

4 RESULTS

4.1 Temperature distributions

In Paper I, we have calculated a temperature in the NS crust and on its surface for pure-dipolar, pure-quadrupolar magnetic fields and their coaxial superpositions. In this work, we have obtained the temperature distributions for non-coaxial superpositions of core-dipolar and quadrupolar fields and have built thermal blackbody light curves, which correspond to the obtained temperature distributions. Because there is no physical constraint, which prohibit the rotation of one field multipole from another one, inclusion of a quadrupolar component in addition to the dipolar one leads us to consideration of two more physical parameters, which affect the spatial temperature distribution: an angle between the dipolar and quadrupolar components Θ_b and a relation between the polar inductions of the components $\beta = B_{pq}/B_{pd}$, which determines the 'strength' of 3D effects. The first (and obvious) conclusion is, that if $\beta \ll 1$, then the temperature approaches to a pure-dipolar configuration, and when $\beta \gg 1$, a pure-quadrupolar one is observable.
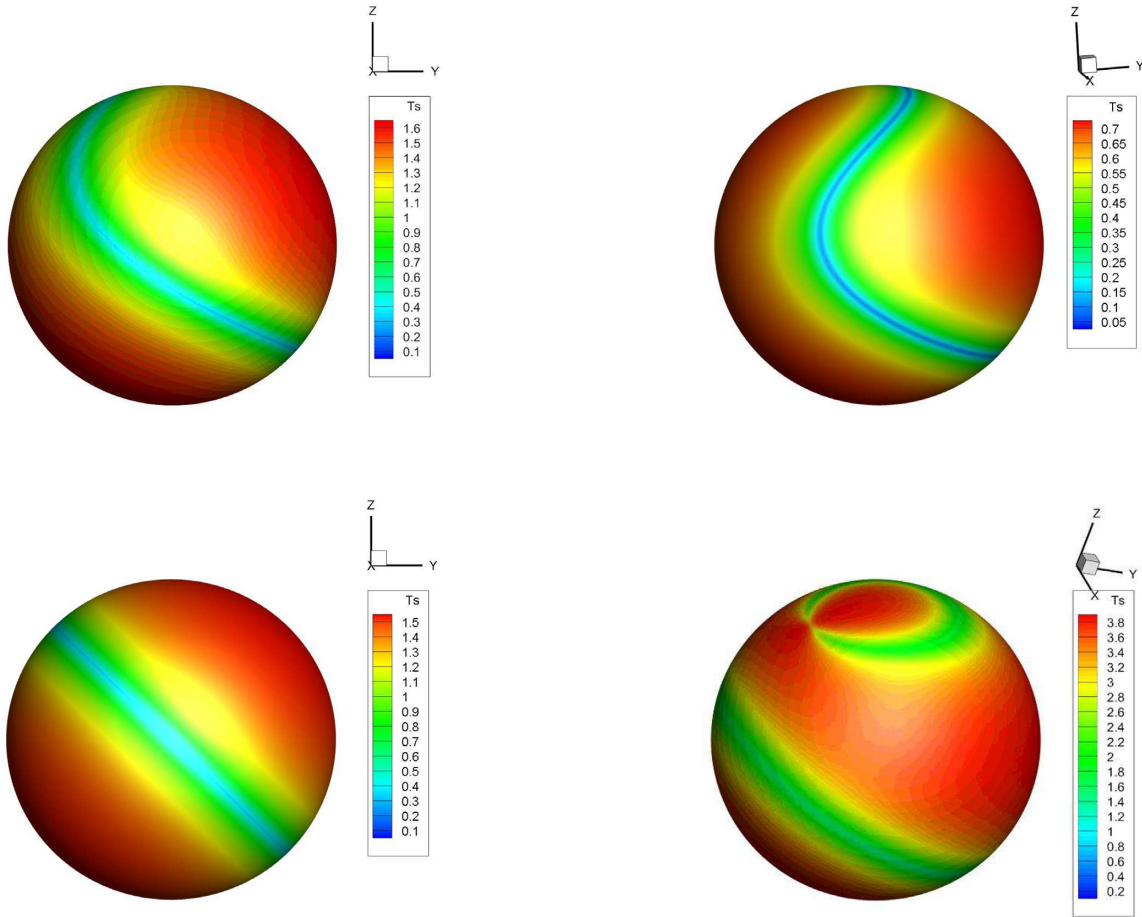
In Fig. 1, temperature distribution in the NS crust is shown for magnetic the dipole and quadrupole, which are rotated on an angle
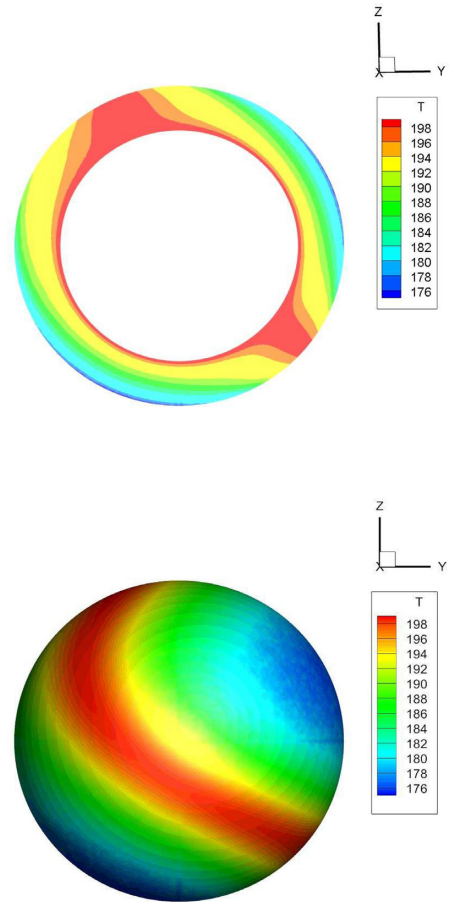
Figure 1. Temperature distribution (in units of 10^6 K) in the NS crust for quadrupolar and dipolar magnetic fields with polar inductions $B_{pq} = 5 \times 10^{12}$ G and $B_{pd} = 1 \times 10^{13}$ G correspondingly ($\beta = 0.5$). Magnetic axes are rotated from each other to the angle $\Theta_b = \pi/4$, hereinafter a quadrupolar axis if fixed along Z-axis, and dipolar component is rotated on plots. The core temperature is $T_{core} = 2 \times 10^8$ K. Upper picture – cross-section in Z–Y plane (the thickness of the crust is four times stretched for better visualization), lower one – the NS crust surface.

$\Theta_b = \pi/4$ from each other, and the quadrupolar strength at the quadrupole magnetic pole is a half from the dipolar one, $\beta = 0.5$. The crustal temperature distribution is inverted in comparison to the surface one, i.e. the crust temperature is smaller in regions, where the magnetic field is at least radial, and larger in the regions with an almost tangential field. The cause is as follows. The heat flux is suppressed most crucially in the envelope, where the magnetization parameter $\omega\tau \gg 1$. The suppressed heat flux from the envelope in the NS regions with the tangential field (equatorial regions) causes decrease of a temperature gradient in the crust, so that a variation of the crust temperature on the magnetic poles, where the field lines are radial, is higher, than on the equator. A temperature variation in the crust is less than 20 per cent of its value.

The surface temperature distribution, which corresponds to the crustal temperature from Fig. 1, is presented in Fig. 2 (upper panel) together with the surface temperature of the NS without the quadrupole field (lower panel). A minimal temperature is approximately 3×10^5 K, and a maximum one is near 1.6×10^6 K. In a pure-dipole case, the surface temperature distribution is represented by two hot polar caps and a cold ring-shaped 'belt'. A 'switching on' of the quadrupolar field effects on the heat transfer as follows. If the parameters $\beta < \sim 1$ and $\Theta_b \neq 0$, the belt shape becomes irregular,

Figure 2. Surface temperature distribution (in units of 10^6 K) for the same parameters as in Fig. 1 (upper panel) and for the NS without the quadrupolar field (lower panel).

Figure 3. Surface temperature distributions (in units of 10^6 K) with parameters $\beta = 0.75$, $T_{core} = 5 \times 10^7$ K and $\Theta_b = \pi/3$ (upper panel) and $\beta = 1$, $T_{core} = 5 \times 10^7$ K and $\Theta_b = \pi/6$ (lower panel). Dipolar component $B_{pd} = 1 \times 10^{13}$ in both cases.

and also the belt is broaden from the one side in comparison to the pure-dipolar configuration. Hot polar caps are not located in antipodal positions in such case, and they have different sizes as well, resembling RX J0720.4−3125 (Haberl 2007). The presence of the quadrupolar field decreases slightly an effective temperature of the NS. Thus, the cold region is larger, than in a pure-dipolar case.

In Fig. 3, the temperature distributions are shown for the different β and Θ_b as well as for different core temperatures T_{core}, which correspond to various NS ages. With increasing of the quadrupole field, the second belt appears, when $\beta \sim 0.9$ for the moderate angles $\Theta_b \sim \pi/6$, and on practice, when $\beta \gtrsim 1.5$, the temperature approaches to the pure-quadrupolar one. For the angles $\Theta_b \lesssim \pi/2$ the shape of the belt takes away more and more from a circular one with increasing of β, getting a shape of a 'jaw', and for $\beta \gtrsim 1.5$ (1.5 for $\Theta_b = \pi/3$) it transforms into the shape of two belts. Also we note here, that our numerical solution is even with respect to a secant plane that passes through the dipolar and quadrupolar axes.

According to 2D cooling calculations by Aguilera et al. (2008), $T_{core} = 2 \times 10^8$ and 5×10^7K correspond to NS ages ∼500 and ∼10^4−10^5 yr, while $T_{core} = 1 \times 10^9$ K corresponds to the NS age ∼1 yr, due to NS cooling by neutrinos emitted from the NS core, which do not disturb the radiation flux. Neutrino emitted from the crust itself could change its temperature distribution, and influence the thermal flux. Our calculations with the highest core temperature ($T_{core} = 1 \times 10^9$ K) should be considered as model example, because we have not included neutrino losses in the crust, although they

are not-negligible. Nevertheless, the surface temperature distribution will not be distorted significantly. The neutrino losses in the crust at such temperatures may cause some redistribution of the crustal temperature in accordance with inclusion of different cooling processes on ρ−T plane, but the part of the neutrino flux emitted from the crust is much smaller than the NS radiation flux, so that the surface temperature is not affected significantly by neutrinos as well as the shape of its thermal light curve.

During a cooling of the NS, the surface temperature anisotropy is amplified. Thus, when the core temperature $T_{core} = 1 \times 10^9$ K, a ratio between the hottest and coldest temperatures is $T_h/T_c \sim 2.5$, and when the core temperature cools to 5×10^7 K, it equals to $T_h/T_c \sim 7$. The magnetization parameter $\omega\tau$ is weakly temperature-independent, and thus we have obtained in our assumptions, that the temperature distributions have the same topology during an NS thermal evolution, if the magnetic dissipation effects are not included.

4.2 Observational manifestations

A modelling of thermal light curves from the rotating magnetized NSs (particularly from XDINSs and X-ray pulsars) is a pretty studied topic. A thermal emission from compact object was considered by a long list of authors (e.g. by Greenstein & Hartke 1983 without general relativity, and by Pechenik, Ftaclas & Cohen 1983; Page 1995; Page & Sarmiento 1996; Zane & Turolla 2006; Turolla & Nobili 2013

with taking into account light bending effects). We have examined observational manifestations from the obtained surface temperature distributions using a simple composite blackbody model. The thermal energy flux is defined in a Newtonian space–time as follows:

$$dF = \frac{2\pi}{c^2 h^3} \frac{R_{\mathrm{NS}}^2}{D^2} \left[\int\limits_{\cos\theta > 0} dS \cos\theta \, I_E(E, T(\theta, \varphi)) \right]$$
$$\times E^3 \exp^{-N_{\mathrm{H}}\sigma(E)} A(E) \, dE \, dt, \tag{15}$$

where $I_E = \left(\exp\left(\frac{E}{k_{\mathrm{B}}T}\right) - 1 \right)^{-1}$ is Planck distribution function, E is a photon energy, θ and φ are azimuth and polar angles correspondingly, D is a distance from the NS to an observer, and $A(E)$ is an effective detector area. We do not consider a detector response in this paper and assume, that the detector has a unit area. An interstellar absorption is taken into account by the term $\exp[-N_{\mathrm{H}}\sigma(E)]$, where N_{H} is a hydrogen column density between the NS and observer, and $\sigma(E)$ is an effective absorption cross-section (Morris & McCammon 1983). Throughout this part of our work, we consider $N_{\mathrm{H}} = 10^{20}$ cm^{-2}. An expression in square brackets in (15) has to be integrated over the surface of a visible hemisphere, and after that dF is integrated over the energies of the photons to obtain a phase-dependent light curve.

General relativistic effects are sufficient for the compact objects. A rigorous relativistic theory of a light propagation near the compact object was developed by Pechenik et al. (1983). In real conditions of the NS, the effects of the general relativity are pronounced mostly by a redshift of the photon energy and a deviation of the photon trajectory from the straight line. The latter effect manifests itself as follows. The ray, which leaves the surface with an angle θ' to the normal to the NS surface, will be bend, and at the infinity this angle will be $\theta > \theta'$ for the observer. Thus, more than a hemisphere is observable, and an effective visible NS radius is more, than the exact one. A simple, but good approximate formula for the relation between θ and θ' was proposed by Beloborodov (2002), and we use it in further calculations:

$$1 - \cos\theta' = (1 - \cos\theta)(1 - x_{\mathrm{g}}), \tag{16}$$

where $x_{\mathrm{g}} = \frac{2GM_{\mathrm{NS}}}{c^2 R_{\mathrm{NS}}}$. With the inclusion of the described effects in the considered model, the energy flux is written as follows:

$$dF = \frac{2\pi}{c^2 h^3} \frac{R_{\mathrm{NS}\infty}^2}{D^2} \left[\int\limits_{\cos\theta' > 0} dS \cos\theta' \, I_E(E_\infty(1 - x_g)^{-1/2}, T) \right]$$
$$\times E_\infty^3 \exp^{-N_{\mathrm{H}}\sigma(E_\infty)} A(E_\infty) \, dE_\infty \, dt_\infty. \tag{17}$$

In the formula above, $E_\infty = E\sqrt{1 - x_{\mathrm{g}}}$ is a redshifted energy, an effective NS radius is equal to $R_{\mathrm{NS}\infty} = R_{\mathrm{NS}}/\sqrt{1 - x_{\mathrm{g}}}$, and term $dt_\infty = dt/\sqrt{1 - x_{\mathrm{g}}}$ corresponds to a time dilation near the NS. The value of θ' is obtained from (16), and the integration of the expression in the square brackets should be done over the visible part of the surface. We consider an energy band of the *XMM–Newton* EPIC-pn detector, so that $E_{\min} = 0.15$ keV, and $E_{\max} = 1.5$ keV.

During observation of the thermal emission from the rotating magnetized NS, pulsations of the visible flux arise. To measure their strength, let us introduce a so-called pulsed fraction (PF):

$$\mathrm{PF} = \frac{F_{\max} - F_{\min}}{F_{\max} + F_{\min}}, \tag{18}$$

where $F_{\max}$ and $F_{\min}$ are the values of the maximal and minimum fluxes of energy (the fluxes of photon counts may be considered for the X-ray sources as well).

In the absence of the quadrupolar component, the pulse profile is symmetric and sinusoidal, and light curve can be either two-peaked (both magnetic poles are visible) or one-peaked (one precessing pole

is visible). Also we introduce here two angles, which characterize a light curve: an angle between the rotational an the dipolar axes α_{d}, and an angle between the rotational axis and a line of sight of the observer ζ. It was noticed by Greenstein & Hartke (1983), that for pure-dipolar magnetic field configurations, when $\alpha_{\mathrm{d}} + \zeta \le \pi/2$, then the light curve is one-peaked, and else, it is two-peaked. General relativistic effects make this conclusion more strict (Page 1995). Inclusion of the quadrupolar component adds one more degree of freedom in a space of positions for the axes, which characterize the light curve, so it makes its analysis much more complicated. Thus, we consider only two limits: the first case (Case 1) is when all three axes – rotational, dipolar, and quadrupolar – are in the same plane, and the second one (Case 2) is when both dipolar and quadrupolar axes are on the line of sight of the observer in some moments of time during rotational period, so that $\alpha_{\mathrm{d}} = \alpha_{\mathrm{q}}$, where α_{q} is an angle between the rotational and quadrupolar axes (e.g. when magnetic axes are in the equatorial plane with respect to the rotational one). Also, we restrict ourselves with a constraint $\alpha_{\mathrm{d}} = \zeta$, unless otherwise specified.

In Fig. 4, the light curves for the orthogonal rotator ($\alpha_{\mathrm{d}} = \zeta = \pi/2$) are presented for the different temperature distributions from the previous subsection for the both limits for the positions of the axes and for the pure-dipolar magnetic field configurations (black lines). When all three axes are in the same plane (blue lines, Case 1), the main indicator of an existence of the quadrupolar field is as follows. The light curve changes slightly from the dipolar ones in the absence of the second cold belt in the temperature distribution (the first two pictures). One peak is tighten, and the second one is broaden in comparison to the pure-dipolar case. PF decreases slightly, e.g. it is 5.1 per cent for the pure-dipole field and PF = 4.2 per cent for the first picture in Fig. 4, then $T_{\mathrm{core}} = 5 \times 10^7$ K. Table 1 gives information about the maximum pulsed fractions for the different light curves. Pulse profiles are symmetric in the Case 1, because of the parity of the solution with respect to the secant plane, which is built on the magnetic axes, so that the light curve has a mirror symmetry at a half period. The third picture from Fig. 4 corresponds to the temperature distribution, where the second cold belt appeared, so that an additional lay-down is observable instead of the second peak.

More interesting situation is provided for the Case 2 (red lines): the symmetry of the pulse profiles is broken, and light curves can take various shapes. Moreover, the pulsations are amplified sufficiently, from 4 per cent up to 17 per cent on the upper panel of Fig. 4. Perhaps, a red line on this picture from Fig. 4 may describe qualitatively the light curve from RX J0420.0−5022 (Haberl 2004). Its PF = 14.2 per cent, and a pulse shape is close to the one observed by the *XMM–Newton*. Also, it should be mentioned that all the synthesized light curves have become one-peaked due to the effects of general relativity. A dashed line on the middle panel of Fig. 4 correspond to the light curve in a flat space–time, and it is two-peaked. The light bending effects have 'blurred' the pulse profile, making two peaks merge into one.

We have considered the effect of the non-coaxial quadrupolar field on the one-peaked light curves, i.e. on the curves, on which only one polar cap is visible for the pure-dipolar magnetic field. We still consider two limits for the positions of the quadrupolar axis in the one-peaked case as well as for two peaked light curves. In Fig. 5, the light curves for Case 1 are presented for different positions of the quadrupolar field. In comparison to the light curve in the pure-dipolar case (black line), a presence of the quadrupole requires to consider more cases of position of the observer and the quadrupole. The quadrupolar field makes one hot polar cap 'smaller' (those one, where dipolar field lines directed *from* the NS surface *to* the core), while the second cap remains at least the same or becomes larger
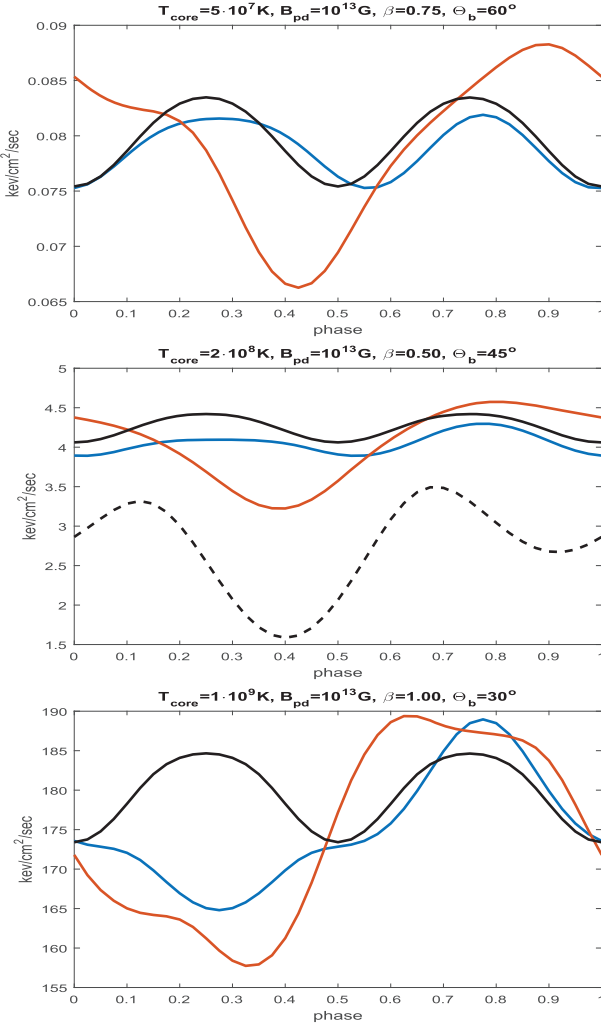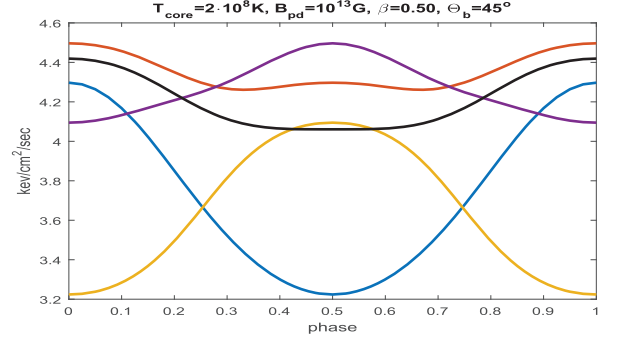
Figure 4. Light curves for the different T_{core}, β, and Θ_b (ones from Figs 2 and 3) for an orthogonal rotator ($\alpha_d = \zeta = \pi/2$). Blue lines correspond to the case, when rotational, dipolar, and quadrupolar axes are in the same plane, red ones correspond to the case, when $\alpha_q = \alpha_d$, so both magnetic axes are visible for the observer. Black lines correspond to the light curves from the NS with a purely dipolar field. A dashed black line is the light curve from the Case 2, but without taking into account light bending effects.

Table 1. PFs (per cent) that correspond the two-peaked light curves from Fig. 4.

	$\beta = 0.75$ $\Theta_b = 60°$	$\beta = 0.50$ $\Theta_b = 45°$	$\beta = 1.00$ $\Theta_b = 30°$
Dipole	5.1	4.2	3.1
Case 1	4.2	4.9	6.8
Case 2	14.2	17.2	9.1

due to a shift of a belt (Page & Sarmiento 1996; Paper I) and its curvature, so that the caps are distinguishable, one from each other. If $\Theta_b = 0$, then only two types of the light curves describe emission from poles, if $\alpha_d = \zeta$, and when the angle Θ_b between components is not equal to zero, the position of the quadrupole with respect to the dipole and the observer leads to four different types of the light curves. All the synthesized light curves are symmetric, and PF can be amplified up to 14.7 per cent for the smaller cap in comparison to the $PF = 4.2$ per cent for the pure dipole, and the larger cap is
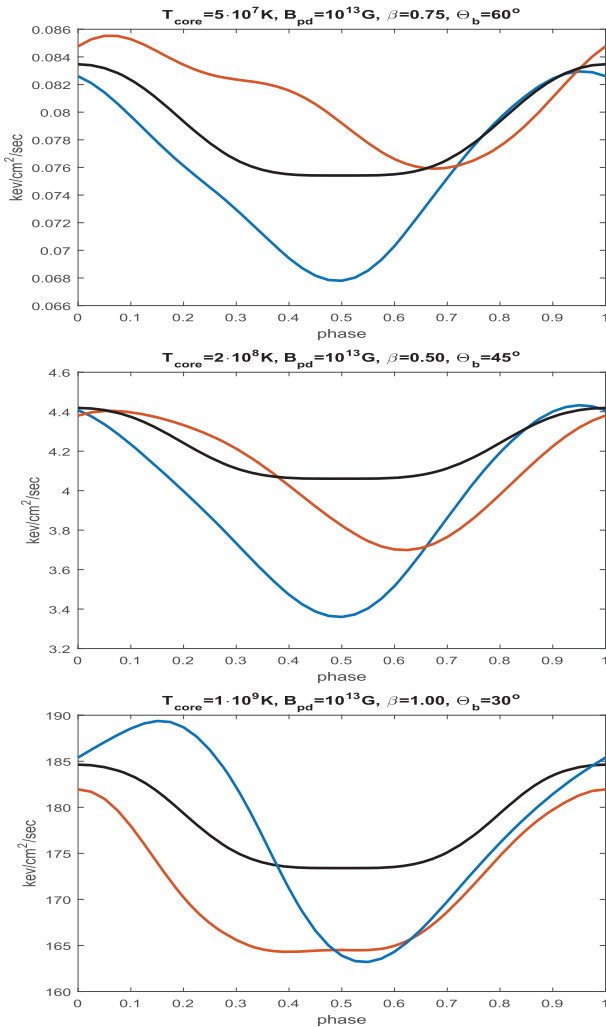

Figure 5. One-peaked light curves for the case, when all axes are in the same plane for the different positions of the magnetic component to each other. Physical parameters are: $T_{core} = 2 \times 10^8$ K, $B_{pd} = 10^{13} G$, $\beta = 0.50$, and $\Theta_b = 45°$ (Fig. 2). Black lines correspond to the pure-dipole. Coloured lines correspond to the different positions of the quadrupolar component: blue and yellow lines correspond to the smaller polar cap, while red and violet ones show the light curves for the larger polar cap.

at least indistinguishable for the observer from the pure-dipolar one by its thermal emission. Moreover, PF can be amplified by different physical processes (e.g. by inclusion of an absorption line in the spectrum, see review by Turolla (2009) about XDINSs as well as a paper by Rigoselli et al. (2019), where the recently discovered and fitted thermal component of PSR J0726−2612 shows strong pulsations), so that an absence of quadrupolar features on the curves may make their analysis more difficult.

In Fig. 6, the light curves for the Case 2 are shown, where the blue lines correspond to the smaller caps, while the red ones correspond to the larger caps. For both polar caps, the pulsations are amplified (see Table 2 for the PF) in comparison to the NS with the purely dipolar field. When the belt in the temperature distribution is the only one, one side of the pulse profile looks similar to a straight line, when the smaller cap is visible, and the curve takes an irregular shape, when the larger cap is observed. This linear dependence of an observed flux on the rotation phase makes the quadrupolar field to be distinguishable. For the star with two cold belts the pulse minimum is shifted from the half period on the light curve, if the energy has maxima on the boundaries of the curve picture (a blue line on the lowest panel of Fig. 6), so that one slope on the light curve is more narrow, than the other one. Such skewness in the pulse profile is inherent to RX J0806.4−4123 (see fig. 4 in Haberl 2004).

The latter situation shows itself more pronounced, when $\alpha_d \neq \zeta$. Although we consider only $\alpha_d = \zeta$, this constraint may be artificial, and some types of light curves can be missed. For example, we have calculated the light curve for the position of the dipolar component, which differs from the viewing position (Fig. 7). Such case may provide very non-symmetric pulse profile, about 70 per cent of the flux dependence on the phase is described by a slope linear function. This feature on the light curve may indicate an existence of the second belt, so it corresponds to the strong quadrupolar component.

We do not affirm that the synthesized light curves fit all the observed properties of the data from RX J0420 and RX J0806, because we have not taken into account, at least, absorption features. It was done properly by Zane & Turolla (2006) using population analysis of models with coaxial dipole-plus-quadrupole fields. The calculated light curves for the NS with non-coincident magnetic axes of dipole and quadrupole can provide similar features as the listed sources. Our model also provides non-antipodal hot caps in the NS surface temperature distributions, which is possibly can be applied to RX J0720. To construct the curves that fit the real data, the

Figure 7. A light curve for the temperature distribution from the lower panel of Fig. 3. The viewing angle is $\zeta = 45°$, and $\alpha_d = 63.5°$, $\alpha_q = 45°$.

model of the thermal structure of the outer envelope, which was built and discussed in Paper I, where we had calculated axisymmetric heat transfer. We have obtained the temperature distributions in the NS crust and on its surface, using the original numerical technique and analytically obtained tensorial electron thermal conductivity coefficient by Bisnovatyi-Kogan & Glushikhina (2018b).

For the computed surface temperature distributions, we have built thermal light curves using a composite blackbody model. The main purpose of this part of our study is to find some qualitative features on the synthetic light curves, which may indicate the non-coaxial field. Presence of the non-coaxial quadrupolar component may affect the light curves by strengthen the pulsations of an observable flux and changing the shape of the pulse profile, as well as making it non-symmetric. Existence of a quadrupolar component in the magnetic field can be detectable, because the synthesized light curves differ both from the pure-dipolar ones and ones with inclusion of the coaxial toroidal or crustal field (Geppert et al. 2006; Perez-Azorin et al. 2006), extending the 'zoo' of observational properties from thermally emitting NSs.

Figure 6. Light curves for the different T_{core}, β, and Θ_b for $\alpha_d = \zeta = \pi/4$ and $\alpha_q = \alpha_d$ (ones from Figs 2 and 3). Blue lines correspond to the case, when only the 'smaller' pole, and red ones correspond to the 'larger' one. Black lines correspond to the light curves from the NS with a purely dipolar field.
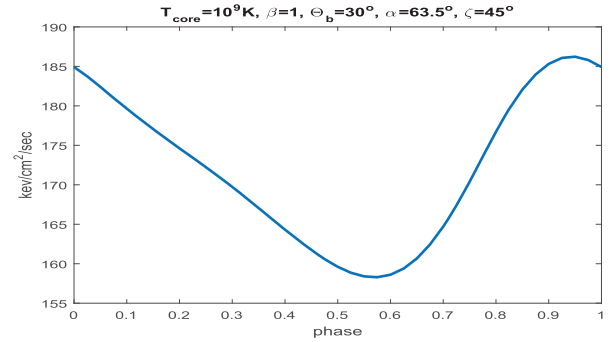
Table 2. PFs (per cent) that correspond to the two-peaked light curves from Fig. 6 for the dipolar field (black lines) and for the 'larger' (red lines) and 'smaller' (blue lines) hot caps.

	$\beta = 0.75$ $\Theta_b = 60°$	$\beta = 0.50$ $\Theta_b = 45°$	$\beta = 1.00$ $\Theta_b = 30°$
Dipole	5.1	4.2	3.1
'Larger' pole	10.0	13.8	7.4
'Smaller' pole	6.1	8.69	5.1

population analysis should be done like in Zane & Turolla (2006). For 3D calculations, it may be computationally expensive.

5 CONCLUSIONS

In this work, we have studied the three-dimensional effects of the anisotropic heat transfer in outer layers of the neutron star with the inclusion of the simplest core-configurations of dipole-plus-quadrupole magnetic fields. We have self-consistently solved the stationary 3D heat transfer equation in the NS crust adopting our

ACKNOWLEDGEMENTS

DATA AVAILABILITY

The data underlying this article will be shared on reasonable request to the corresponding author.

REFERENCES

Aguilera D. N., Pons J. A., Miralles J. A., 2008, A&A, 486, 255
Antia H. M., 1993, ApJS, 84, 101
Ardeljan N. V., Kosmachevskii K. V., 1995, Comput. Math. Modelling, 6, 209
Baym G., Pethick C., Sutherland D., 1971a, ApJ, 170, 306
Baym G., Bethe H., Pethick C., 1971b, Nucl. Phys. A, 175, 225
Beloborodov A. M., 2002, ApJ, 566, L85
Berestetskii V. B., Lifshitz E. M., Pitayevskii L. P., 1989, Quantum Electrodynamics. Pergamon, Oxford
Bisnovatyi-Kogan G. S., 2001, Stellar Physics I: Fundamental Concepts and Stellar Equilibrium. Springer-Verlag, Berlin
Bisnovatyi-Kogan G. S., Glushikhina M. V., 2018a, Plasma Phys. Rep., 4, 355
Bisnovatyi-Kogan G. S., Glushikhina M V, 2018b, Plasma Phys. Rep., 44, 1114

Bisnovatyi-Kogan G. S., Kulikov Yu. N., Chechetkin V. M., 1976, SvA, 20, 552

Blandford R. D., Applegate J. H., Hernquist L., 1983, MNRAS, 204, 1025

Blinnikov S. I., Dunina-Barkovskaya N. V., Nadyozhin D. K., 1996, ApJS, 106, 171

Braginskii S. I., 1957, Sov. Phys. JETP, 6, 358

Chabanat E., Bonche E., Haensel E., Meyer J., Schaeffer R., 1997, Nucl. Phys. A, 627, 710

Chabrier G., Potekhin A. Y., 1998, Phys. Rev. E, 58, 4941

Douchin F., Haensel P., 2001, A&A, 380, 151

Flowers E., Itoh N., 1976, ApJ, 206, 218

Geppert U., Kuker D., Page D., 2004, A&A, 426, 267

Geppert U., Kuker D., Page D., 2006, A&A, 457, 937

Glushikhina M. V., 2020, Plasma Phys. Rep., 46, 157

Greenstein G., Hartke G. J., 1983, ApJ, 271, 283

Gudmundsson E. H., Pethick C. J., Epstein R. I., 1983, ApJ, 272, 286

Haberl F. et al., 2004, A&A, 424, 635

Haberl F. et al., 2007, Ap&SS, 308, 181

Kondratyev I. A., Moiseenko S. G., 2019, J. Phys.: Conf. Ser., 1163, 012069

Kondratyev I. A., Moiseenko S. G., Bisnovatyi-Kogan G. S., Glushikhina M. V., 2020, Astron. Rep., 64, 226 (Paper I)

Landau L. D., Lifshitz E. M., 1988, Field Theory. Pergamon, Oxford

Morris R., McCammon D., 1983, ApJ, 270, 119

Page D., 1995, ApJ, 442, 273

Page D., Sarmiento A., 1996, ApJ, 473, 1067

Page D., Geppert U., Weber F., 2006, Nucl. Phys. A, 777, 497

Pechenik K. R., Ftaclas C., Cohen J. M., 1983, ApJ, 274, 846

Perez-Azorin J. F., Miralles J. A., Pons J. A., 2006, A&A, 451, 1009

Pons J. A., Vigano D., 2019, Living Rev. Comput. Astrophys., 5, 3

Pons J. A., Walter F. M., Lattimer J. M., Prakash M., Neuhauser R., An P., 2002, ApJ, 564, 981

Pons J. A., Miralles J. A., Geppert U., 2009, A&A, 496, 207

Potekhin A. Y., Yakovlev D. G., 2001, A&A, 374, 213

Potekhin A. Y., Chabrier G., Yakovlev D. G., 1997, A&A, 323, 415

Potekhin A. Y., Chabrier G., Yakovlev D. G., 2007, Ap&SS, 308, 353

Potekhin A. Y., Pons J. A., Page D., 2015, Space Sci. Rev., 191, 239

Rigoselli M., Mereghetti S., Suleimanov V., Potekhin A. Y., Turolla R., Taverna R., Pintore F., 2019, A&A, 627, A69

Rybicki G. B., Lightman A. P., 2004, Radiative Processes in Astrophysics. Wiley-VCH, Verlag GmbH & Co. KGaA

Schwarzschild M., 1958, Structure and Evolution of the Stars. Princeton Univ. Press, Princeton, NJ

Silant'ev N. A., Yakovlev D. G., 1980, Ap&SS, 71, 45

Turolla R., 2009, ASSL, 357, 141

Turolla R., Nobili L., 2013, ApJ, 768, 147

Urpin V., Yakovlev D. G., 1980, SvA, 24, 303

Van Riper K. A., 1988, ApJ, 329, 339

Vigano D., Rea N., Pons J. A., Aguilera D. N., Miralles J. A., 2013, MNRAS, 434, 123

Yakovlev D. G., Urpin V. A., 1980, SvA, 57, 526

Zane S., Turolla R., 2006, MNRAS, 366, 727

APPENDIX A: RADIATIVE OPACITIES

Radiative opacity is represented mostly by electron Thompson scattering, free–free, and bound–free absorption. In an absence of the magnetic field in non-relativistic limit, Thompson opacity is given by Berestetskii, Lifshitz & Pitayevskii (1989):

$$K_{\mathrm{Th}} = \frac{n_e \sigma_{\mathrm{T}}}{\rho} = \frac{8\pi}{3} \left(\frac{e^2}{m_e c^2} \right)^2 \frac{n_e}{\rho}, \tag{A1}$$

where σ_{T} is a Thompson scattering cross-section and $\frac{e^2}{m_e c^2}$ is a classical electron radius.

A cross-section of a free–free absorption with taking into account spontaneous and stimulated emission in non-relativistic limit in local thermodynamic equilibrium is given by

$$\sigma_{\mathrm{aff}}^* = \frac{4\pi}{3\sqrt{3}} \frac{Z^2 e^6}{m_e^2 ch v v^3} g_{\mathrm{ff}} \left(1 - e^{-h\nu/k_{\mathrm{B}}T} \right), \tag{A2}$$

where v is an electron velocity, ν is a photon frequency, g_{ff} is a Gaunt factor, which takes into account quantum corrections to classical formula. To obtain the absorption coefficient (Bisnovatyi-Kogan 2001) on one frequency, we have to average (A2) with a Fermi–Dirac statistics:

$$\alpha_{\mathrm{ff}}^\nu = \frac{8\pi m_e^3}{Am_u h^3} \int_0^\infty \frac{\sigma_{\mathrm{aff}}^* v^2 \, \mathrm{d}v}{1 + \exp(\frac{mv^2}{2k_{\mathrm{B}}T} - \chi)} q_{\mathrm{ff}},$$

$$q_{\mathrm{ff}} = \left(1 + \exp\left(\chi - \frac{h\nu}{k_{\mathrm{B}}T} - \frac{mv^2}{2k_{\mathrm{B}}T} \right) \right)^{-1},$$

here m_u is an atomic mass unit, and factor q_{ff} determines a fraction of vacant electron states in a degenerate gas. An integration gives

$$\alpha_{\mathrm{ff}}^\nu = \frac{4\pi}{3\sqrt{3}} \frac{8\pi Z^2 e^6}{Am_u ch^4 v^3} g_{\mathrm{ff}} k_{\mathrm{B}} T \log \left(\frac{e^\chi + 1}{e^{\chi - h\nu/k_{\mathrm{B}}T} + 1} \right). \tag{A3}$$

To obtain the opacity expression for free–free transitions, it is necessary to derive the Rosseland meaning (e.g. Rybicki & Lightman 2004) from (A3) in the following manner:

$$K_{\mathrm{ff}} = \frac{\int_0^\infty \frac{1}{\alpha_{\mathrm{ff}}^\nu} \frac{\mathrm{d}B_\nu}{\mathrm{d}T} \, \mathrm{d}\nu}{\int_0^\infty \frac{\mathrm{d}B_\nu}{\mathrm{d}T} \, \mathrm{d}\nu}.$$

In the formula above, $B_\nu(T) = \frac{2h\nu^3}{c^2} \frac{1}{e^{h\nu/k_{\mathrm{B}}T} - 1}$ is an intensity of equilibrium Planck blackbody radiation. The Rosseland mean opacity for non-degenerate case reads (Bisnovatyi-Kogan 2001)

$$K_{\mathrm{ff}}^{\mathrm{nd}} = 4.34 \times 10^{22} \frac{\rho}{T^{7/2}} \frac{Z^2}{A} \, \mathrm{cm}^2 \, \mathrm{g}^{-1}, \tag{A4}$$

and in strongly degenerate limit the value of K_{ff} is given by

$$K_{\mathrm{ff}}^{\mathrm{sd}} = 0.036 \frac{32\pi^2}{3\sqrt{3}} \frac{e^6 g_{\mathrm{ff}}}{m_u ch k_{\mathrm{B}}^2} \frac{Z^2}{AT^2}. \tag{A5}$$

A cross-section of bound–free absorption is given by the following formula in the non-relativistic limit (e.g. Bisnovatyi-Kogan 2001):

$$\alpha_{\mathrm{bf}}^\nu = \frac{4}{3} \sqrt{\frac{2\pi}{3}} \frac{e^6 h^2}{m_e^{3/2} cm_u (k_{\mathrm{B}}T)^{7/2}} \frac{Z^2}{A} n_e g_{\mathrm{bf}}$$

$$\times \left[\frac{1}{n} \frac{E_{\mathrm{b}}}{k_{\mathrm{B}}T} \exp^{E_{\mathrm{b}}/k_{\mathrm{B}}T} \left(\frac{k_{\mathrm{B}}T}{h\nu} \right)^3 q_{\mathrm{bf}} \right],$$

$$E_{\mathrm{b}} = \frac{2\pi^2 m_e Z^2 e^4}{h^2 n^2},$$

$$q_{\mathrm{bf}} = \left(1 + \exp\left(\chi - \frac{h\nu}{k_{\mathrm{B}}T} + \frac{E_{\mathrm{b}}}{k_{\mathrm{B}}T} \right) \right)^{-1}, \tag{A6}$$

where E_{b} is an energy value of an energy level of a bounded electron in a hydrogen-like ion, n is an energy level number, g_{bf} is a Gaunt factor, and q_{bf} is a degeneracy correction factor. To obtain the opacity coefficient, we have to summarize an expression in square brackets of α_{bf}^ν in (A6) over all bound states and make a Rosseland averaging of this expression. For non-degenerate electrons, we use an expression of K_{bf} from the book by Bisnovatyi-Kogan (2001):

$$K_{\mathrm{bf}}^{\mathrm{nd}} = 7.23 \times 10^{24} \frac{\rho}{T^{7/2}} \frac{Z^2}{A} \frac{g_{\mathrm{bf}}}{t} \mathrm{cm}^2 \, \mathrm{g}^{-1}, \tag{A7}$$

where factor $\frac{t}{g_{\mathrm{bf}}}$ takes values from 1 to 10. With increasing the density the electron gas in the NS outer envelope goes fast to a strong degeneracy. To take into account an influence of the degeneracy on

the bound-free absorption, let us write a sum α_{bf}^ν in (A6) over the electron bound states:

$$\alpha_{\mathrm{bf}}^\nu = K_0 \sum_{n=1}^{\infty} \frac{E_{\mathrm{b}}}{n k_{\mathrm{B}} T} \frac{e^{-\chi}}{x^3} \frac{e^x - 1}{e^{x - \frac{E_{\mathrm{b}}}{k_{\mathrm{B}} T} - \chi} + 1}, \qquad (A8)$$

where $K_0 = K_{\mathrm{bf}}^{\mathrm{nd}} t$, and $x = \frac{h\nu}{k_{\mathrm{B}} T}$. In the expression above the chemical potential $\chi \gg 1$, and mostly only very hard photons in a 'tail' of a Planck spectrum are absorbed effectively, and they will not contribute sufficiently in the mean opacity. Neglecting an exponent $e^{x - \frac{E_{\mathrm{b}}}{k_{\mathrm{B}} T} - \chi}$ in (A8) and averaging over n and frequencies according to Schwarzschild (1958) for the non-degenerate case, the following expression can be obtained for the degenerate case:

$$K_{\mathrm{bf}}^{\mathrm{sd}} = K_0 e^{-\chi} \frac{g_{\mathrm{bf}}'}{t'}, \qquad (A9)$$

factor $\frac{t'}{g_{\mathrm{bf}}}$ also takes values from 1 to 10. It is seen, that for the case of the degenerate electron gas bf-opacity decreases exponentially with the growth of the density.

To use formulae (A4) and (A5) for the ff-transitions and (A7) and (A9) for the bf-transitions in our calculations, we have to stitch them continuously, for example, in the following way:

$$K_{\mathrm{ff,bf}} = K_{\mathrm{ff,bf}}^{\mathrm{nd}} \frac{1}{1 + e^{m\chi}} + K_{\mathrm{ff,bf}}^{\mathrm{sd}} \frac{e^{m\chi}}{\varepsilon + e^{m\chi}}, \qquad (A10)$$

where m, $\varepsilon > 1$ are numbers, which determine the smoothness of transition from one limit to another. We note, that in $K_{\mathrm{bf}}^{\mathrm{sd}}$ it is necessary to replace $\chi = \frac{\mu_{\mathrm{e}}}{k_{\mathrm{B}} T}$ by its absolute value. Thus, in the absence of magnetic field the value of the radiative opacity is composed of Thompson, free–bound and free–free ones: $K_r(\rho, T)_{\mathrm{B}=0} = K_{\mathrm{Th}} + K_{\mathrm{bf}} + K_{\mathrm{ff}}$.

In presence of the strong magnetic field, the photon opacity is reduced and becomes anisotropic. We have taken into account an effect of the magnetic field on the opacity in the same manner, as in Potekhin & Yakovlev (2001). Authors of that work have built an analytical approximation of numerically obtained magnetic correction factors from Silant'ev & Yakovlev (1980) for Thompson scattering and free–free absorption. The influence of magnetic field on the bound–free opacity is assumed to be the same as on the free–free one.

APPENDIX B: NUMERICAL IMPLEMENTATION

B.1 Operator formulation of the problem

With an approach suggested and discussed in Ardeljan & Kosmachevskii (1995), we have to include boundary conditions in an operator-difference form of a considered problem. Let us write the system of equations (13) in a difference form in a whole region using a cell-node approximation:

$$\begin{cases} \nabla_\times \cdot \kappa^n \cdot \nabla_\triangle T^n + \delta_1 \Phi \cdot \kappa^n \cdot \Phi T^n + \\ + \delta_2 \Phi \kappa^n \cdot \Phi T^n = 0, \\ \delta_1 T^n = T_{\mathrm{core}}, \\ \delta_2 (\kappa^n \cdot \Phi T^n + \vec{n} \sigma T_{\mathrm{s}}^4) = 0, \end{cases} \qquad (B1)$$

where the notations are adopted from (Ardeljan & Kosmachevskii 1995): $\nabla_\times \cdot$ and $\nabla_\triangle$ are difference approximations of differential

divergence and gradient operators, Φ is a boundary operator, it corresponds to a derivation procedure on the boundary. Here operator δ is defined as follows: it equals to 0 in the interior mesh nodes and to 1 on the boundary surface, indexes 1 and 2 correspond the sort of a particular bound, 1 – inner and 2 – outer bound. Index n corresponds to an iteration number in 'time', and $T_{\mathrm{s}}^n = T_{\mathrm{s}}^n(\delta_2 T^{n-1})$. Temperature is defined in the nodes, and magnetic field and density are defined in the cells and boundary nodes of the mesh.

After acting on (B1) with scalar boundary operator and subtracting it from the first equation, we obtain the following system:

$$\begin{cases} \nabla_\times \cdot \kappa^n \cdot \nabla_\triangle T^n + \delta_1 \Phi \cdot \kappa^n \cdot \Phi T^n - \delta_2 \Phi \cdot \vec{n} \sigma T_{\mathrm{s}}^4 = 0 \\ \delta_1 T^n = T_{\mathrm{core}} \end{cases}.$$

After that let us allocate the first (inner) boundary in the first equation from (B1) and multiply the first equation from (B1) by δ_1, and after substituting one equation from another and a substitution the Dirichlet boundary condition on the inner boundary, we can derive the final operator-difference equation:

$$(I - \delta_1) \nabla_\times \cdot \kappa^n \cdot \nabla_\triangle (I - \delta_1) T^n$$
$$+ (I - \delta_1) \nabla_\times \cdot \kappa^n \cdot \nabla_\triangle T_{\mathrm{core}} - \delta_2 \Phi \cdot \vec{n} \sigma T_{\mathrm{s}}^4 = 0, \qquad (B2)$$

where I is a unit operator. A resulting operator equation is a finite-difference approximation of the considered boundary problem (13).

B.2 Algorithm of solving a heat transfer equation in an NS crust

In this work, we look for the stationary solution for the boundary problem (13). This problem has to be solved self-consistently, because surface temperature T_{s} in the outer boundary condition is a function of a temperature in the crust itself. We implemented an iterative procedure of relaxation: the problem is solved with boundary conditions of first type on the inner boundary and of the second type on the outer one n times until inequality $\max\left| \frac{T_{\mathrm{s}}^n - T_{\mathrm{s}}^{n-1}}{T_{\mathrm{s}}^{n-1}} \right| < \epsilon$ is not satisfied, where n is an iteration number, ϵ is a some small number. After each iteration the value of T_{s} is specified with the $T_{\mathrm{s}} - T_{\mathrm{b}}$ relationship with the surface temperature distribution, obtained from the previous iteration. The value T_{s}^0 for the boundary condition on the first iteration is obtained from the initial approach of the crust temperature. In some sense, this procedure is equivalent to a solving a time-dependent heat transfer equation with boundary conditions of the first and the third types, while the value of the heat flux density $\sigma T_{\mathrm{s}}^4(T)$ in the outer boundary condition from (13) is taken from the previous 'time'-step.

On each 'time'-step the system (13) is solved with the Basic operators method, described in Kondratyev et al. (2020).

The operator-difference equation (B2) is non-linear in T^n and should be solved with Newton method of solving systems of non-linear equations, and appeared system of linear algebraic equations on the each Newton method iteration is solved by the iterative Seidel method.

Thus, following the procedure described above, the self-consistent temperature distribution can be found in a crust volume and on the NS surface.

This paper has been typeset from a TEX/LATEX file prepared by the author.